Journal of Environmental Chemical Engineering 12 (2024) 113139

Contents lists available at ScienceDirect

Journal of Environmental Chemical Engineering

journal homepage: www.elsevier.com/locate/jece

Electrochemical treatment coupled with solar light-driven photocatalytic approach: A challenging process in cascade for hydrogen production and wastewater remediation

Ermelinda Falletta [a,b,1], Roberto Bernasconi [c,1], Vincenzo Fabbrizio [a,b], Eleonora Marcolini [a,b], Alessia Giordana [d], Iliyan Boykov Iliev [c], Luca Magagnin [c], Claudia L. Bianchi [a,b,*]

[a] Dipartimento di Chimica, Università degli Studi di Milano, via C. Golgi, 19, Milano 20133, Italy
[b] Consorzio Interuniversitario Nazionale per la Scienza e Tecnologia dei Materiali (INSTM), Via Giusti 9, Firenze 50121, Italy
[c] Dipartimento di Chimica, Materiali e Ingegneria Chimica "Giulio Natta", Politecnico di Milano, via Mancinelli 7, Milano 20131, Italy
[d] Dipartimento di Chimica, Università degli Studi di Torino, via Pietro Giuria 7, Torino 10121, Italy

ARTICLE INFO

Keywords:
Wastewater
H2
Photocatalysis
Electrochemical treatment
Solar light
Solar-driven process

ABSTRACT

This study presents an innovative approach for simultaneous hydrogen production and wastewater remediation, integrating electrochemical treatment with solar light-driven photocatalysis. The research focuses on the use of a noble metal-free cathode, based on a electrodeposited composite of Co_2P and elemental P, for efficient hydrogen generation from simulated wastewater through water splitting. This composite is characterized, in its optimized form, by an overpotential equal to 133.6 mV (at 10 mA cm^{-2}) and by a Tafel slope of 60.5 mV dec^{-1}. Challenges like the high potential required for the Oxygen Evolution Reaction (OER) and the use of expensive noble metals in electrodes are addressed by employing earth-abundant compounds for electrode fabrication. Additionally, the study explores the degradation of diclofenac (DCF) in wastewater, demonstrating that electrochemical treatment alone is insufficient for organic matter removal. Therefore, a coupled process involving a first electrochemical treatment step followed by a photocatalytic process using BiOCl is proposed. Thanks to the exposure of the (110) active face, BiOCl possesses excellent photocatalytic performances even under solar light irradiation. This hybrid approach not only enhances the efficiency of DCF degradation (about 90%) and reaches an organic matter removal of 59%, but it also improves hydrogen production, offering a sustainable solution for energy generation and water purification in the face of increasing global industrialization and water scarcity.

1. Introduction

The rising global population is placing unprecedented pressure on world energy production. In this context, the scientific community and the industrial sector are moving toward the possibility to obtain a carbon-neutral energetic production [1]. In the last decades, renewable energy sources (e.g., wind or solar irradiation) have been increasing. Although this represents a significant step forward, unfortunately, these technologies suffer from several disadvantages, such as intermittency in energy production or the impossibility of storing all the produced energy [2], to mention some of them. In this scenario, hydrogen (H_2) is a promising energy storage medium whose market is expected to increase shortly due to its use as an energy vector in the transportation sector [3]. Currently, ca. 96% of its production is based on non-renewable sources [4] and only 4% comes from water splitting (Eq. 1). Even if this latter is considered a promising method for clean hydrogen generation, it suffers from some limitations, such as the high potential required for Oxygen Evolution Reaction (OER), that occurs in the anodic section limiting the Hydrogen Evolution Reaction (HER) in the cathodic section [5], and the use of expensive noble metals for electrode fabrication [6].

$$\text{Total reaction } H_2O \rightarrow H_2 + 1/2O_2 \quad (1)$$

In acidic solution

$$\text{Cathode } 2H^+ + 2e^- \rightarrow H_2 \quad (2)$$

$$\text{Anode } H_2O \rightarrow 2\,H^+ + 1/2O_2 + 2e^- \quad (3)$$

* Corresponding author at: Dipartimento di Chimica, Università degli Studi di Milano, via C. Golgi, 19, Milano 20133, Italy.
E-mail address: claudia.bianchi@unimi.it (C.L. Bianchi).
[1] Ermelinda Falletta and Roberto Bernasconi equally contributed.

https://doi.org/10.1016/j.jece.2024.113139
Received 3 February 2024; Received in revised form 19 May 2024; Accepted 20 May 2024
Available online 22 May 2024

In alkaline solution

$$\text{Cathode } 2H_2O + 2e^- \rightarrow H_2 + OH^- \quad (4)$$

$$\text{Anode } 2OH^- \rightarrow H_2O + ½\ O_2 + 2e^- \quad (5)$$

To overcome this latter, in the last decades, researchers have been moving toward the development of noble metal-free electrodes mainly based on earth-abundant compounds [7–9]. As a way of example, *Wang et al.*, proposed a robust electrocatalyst based on selenium-enriched nickel selenide for HER [10]. Results showed that the investigated material is characterized by a low overpotential for the HER (125 mV at 10 mA cm^{-2}). Recently, Zhang *et al.*, developed a new noble metal-free cathode for HER based on Mo-doped Co_2FeAl alloys able to work in alkaline conditions for 20 h, displaying a low overpotential of 71 mV when 10 mA cm^{-2} were applied [11].

One of the most promising class of earth-abundant compounds that can be used as electrocatalysts for HER comprises transition metals phosphides [12]. These materials are cheap, easy to manufacture, relatively efficient and highly stable in a wide range of conditions. Most of the literature available addresses the properties of nanostructured binary compounds like Ni-P [13], Co-P [14] or Fe-P [15], but studies on the HER activity of ternary [16] and quaternary phosphides [17] are available as well. The key aspects to boost the applicability of these materials is the development of simple and low cost manufacturing methods, including technologies adapt for roll to roll production and for the direct application of the active layers as thin films. In this context, one of the most promising approaches is probably hydrothermal synthesis. Between the wealth of examples present in literature, it is useful to highlight the work carried out by Cao *et al.* for the production of hierarchical CoP nanostructures [18]. For direct thin films deposition, an interesting strategy is the one proposed by Bernasconi *et al.* Their simple codeposition/annealing route allowed the direct deposition of HER active layers based on Ni-P ad characterized by overpotentials around 170 mV (at 10 mA cm^{-2}) [19,20]. In addition to these considerations on transition metal phosphides, it is worth mentioning that also pure phosphorus, and specifically the red allotrope, is characterized by interesting HER properties [21]. Due to its poor mechanical properties and problematic manufacturability, red P is typically employed supported on a second material or embedded in a composite [22].

Regarding the anodic reaction, the addition of organic species in water, subjected to electrolysis for hydrogen generation causes a reduction in the required overall potential with respect to the one required for the OER [23], facilitating the hydrogen evolution in terms of energy demand. In this regard, the growing population and the exponential global industrialization are putting unprecedented pressure on water resources, generating huge amounts of wastewater contaminated by organic compounds. The treatment of these wastes can represent an important challenge to generate alternative water sources in the current water scarcity scenario [24]. Electrochemical treatment is emerging as a promising tool for wastewater remediation thanks to its high efficiency [25] and versatility [26]. However, different challenges and limitations make its successful implementation difficult [27]. It was demonstrated that the interaction between some classes of contaminants (organic and inorganic species and heavy metals, to mention some of them) and the working electrode can deactivate it [28]. Moreover, solid species or specific by-products can accumulate on the electrode surface, reducing the activity of the overall system [29] and limiting the water decontamination at the same time. Therefore, the combination of electrochemical systems and other processes can represent an effective strategy to reduce these drawbacks and maximize their practical application. In this context, different researchers have investigated the use of electrochemical processes for the wastewater pre- or post-treatment [30]. In this manner, the presence of harmful species, that can compromise the application of mature technologies (i.e., anaerobic – aerobic biological treatment), can be strongly reduced. Pęziak-Kowalska *et al.* [31] performed the degradation of herbicidal ionic liquids (HILS) coupling an EO (1st step) with a biological treatment (2nd step). The results showed that the coupled process leads to a more significant mineralization of the organic compounds present in the waste (57%) compared to the results obtained without any electrochemical step (8%).

Similarly, Ouarda *et al.*, combined a membrane microreactor (MBR) and an EO process to treat simulated hospital wastewater containing drugs. The results showed that when EO is used as post-treatment of the MBR step, pollutants abatement reaches 97% instead of 90% obtained using the EO step in the pre-treatment section [32]. In fact, the removal of specific organic species able to poison the surface of the electrode by filtration (MBR) enhances the life of the electrode itself.

An alternative and intensely investigated approach for wastewater purification is represented by heterogeneous photocatalysis [33]. Thanks to the exploitation of light irradiation in the presence of a proper semiconductor, radical species, like hydroxyl (·OH), peroxyl ($O_2^{\cdot-}$), and hydroperoxide (HO_2·), able to abate organic contaminants are generated [34]. Unfortunately, the abatement of highly contaminated wastewater is not fast enough. Additionally, the adsorption of organic or inorganic by-products generated on the catalyst's surface during the photocatalytic oxidation can reduce its photocatalytic performances. To improve the activity, a higher amount of catalysts is required, reflecting in the increase of the overall cost for the entire treatment [35].

Regarding the photocatalytic active phase, titanium dioxide (TiO_2) was deeply investigated in the environmental remediation field for several years due to its semiconductor properties [36]. Unfortunately, it tends to go through phase transformation from anatase to rutile, thus reducing its photocatalytic behavior [37]. Moreover, TiO_2 has been recently recognized as a potentially carcinogenic substance [38]. Finally, it is activated by UV light, representing only 4% of the entire solar spectrum. Therefore, alternative non-TiO_2-based semiconductors must be found to overcome these limitations. In this regard, Bi-based photocatalysts, in particular bismuth oxyhalides (BiOX, where X = Cl, Br or I), have been recently investigated thanks to their easy synthesis, high chemical stability, unique layer structure, and great lifetime of electric charges after light irradiation [39]. Among them, BiOBr and BiOI are particularly interesting for their narrow band gap (~2.64 eV and ~1.77 eV, respectively) that gives them a strong visible light activity, in contrast to BiOCl characterized by a broad band gap of ~3.3 eV [40]. However, the band gap value is not the unique feature responsible of the photocatalytic activity of this semiconductor. In fact, as reported in the literature [41], the type of crystal facet more exposed in the crystal structure of BiOCl is very significant since each facet possesses different physicochemical properties, included photocatalytic ones. BiOCl characterized by higher exposure of (110) active facet possess excellent photocatalytic performances even under solar light irradiation, because the exposed (110) crystal plane facilitates the migration of holes and reduces the recombination of photogenerated electron–hole pairs [41].

Solar-induced photocatalytic processes are among the greener and most promising technologies for wastewater remediation.

In this regard, Hu *et al.* investigated the use of BiOCl for the atenolol (a kind of beta-blockers) photocatalytic degradation demonstrating high photocatalytic efficiency in 60 minutes of irradiation under simulated natural light [42], whereas Yang and coworkers demonstrated the enhanced photocatalytic activity of BiOCl under solar light when the proper crystal facet (110) is mainly exposed [42].

Based on these premises, it is evident that, in order to return safe water to the environment and at the same time to generate green hydrogen, electrochemical treatment alone may not be sufficient. Hence, coupling this latter with an additional process capable of completing the purification step, such as photocatalysis, can represent an essential and innovative solution that can simultaneously guarantee green hydrogen production and effective abatement of organic contaminants.

This work focuses on the electrochemical hydrogen generation from simulated wastewater using an innovative, cost-effective, noble metals-

free electrode cathode based on Co_2P/P. Indeed, the use of water matrix enriched with organic compounds permits to reduce the potential required for the Oxygen Evolution Reaction (OER) in the anodic section, enhancing the Hydrogen Evolution Reaction (HER) in the cathodic section.The manufacturing route employed for the preparation of the new catalytic material is inspired by the approach followed in literature for the low cost manufacturing of Ni-P based electrocatalysts [19,20]. In analogy, the material is synthesized starting from a nanocomposite deposited in the form of thin film on a substrate. Such composite contains red phosphorus particles dispersed into a Co-P solid solution (Co-P/P). Unlike what done with Ni-P [19,20]; however, the high temperature conversion of the Co-P/P composite into crystalline Co_2P is not completed. On the contrary, the temperature and duration of the heat treatment were carefully tailored to convert only partially the red phosphorus present. The goal is to obtain a nanocomposite that still contains red phosphorus dispersed in a Co_2P matrix. By doing this, the interesting catalytic properties of pure red P [19] can be exploited in combination with those of Co_2P. In addition, the coupling in the cascade of a photocatalytic step has been investigated, as a crucial and strategic approach to enhance pollutant degradation and achieve the main objective of the work: producing green hydrogen from wastewater and degrading organic contaminants. BiOCl having selective (110) crystal facet exposed was selected as a photocatalytic solar light active phase, exploiting its ability to alleviate water contamination. Diclofenac (DCF) was selected chosen not only because it is a model molecule for drugs, but also to investigate the efficiency of the combined system in the presence of wastewater having a certain COD level.

2. Materials and methods

2.1. Chemicals

All chemicals were of analytical grade and purchased from Sigma Aldrich. A Milli-Q® ultra-pure water system from Merck Millipore obtained ultrapure water.

2.2. Materials preparation

2.2.1. Co_2P/P electrode preparation

The manufacturing process for the production of the Co_2P/P active material is schematized in Fig. 1a. Pure copper plates (3 cm × 6 cm) were used as substrates (step I in Fig. 1a).

Their surface was degreased with acetone and the native oxide was removed with a 6.5% HNO_3 solution (10 s immersion time). The following step was the electrodeposition of the Co-P/P composite (step II in Fig. 1a). The following electrolyte was employed: $CoSO_4 \cdot 6\ H_2O$ 80 g L^{-1}, H_3PO_3 15 g L^{-1}, H_3BO_3 24 g L^{-1}, red phosphorus microparticles 0–100 g L^{-1}. After their addition to the electrolytic solution, the red P particles were ball-milled. Initially, the solution was prepared by dissolving only the soluble compounds. Then, the red P particles were

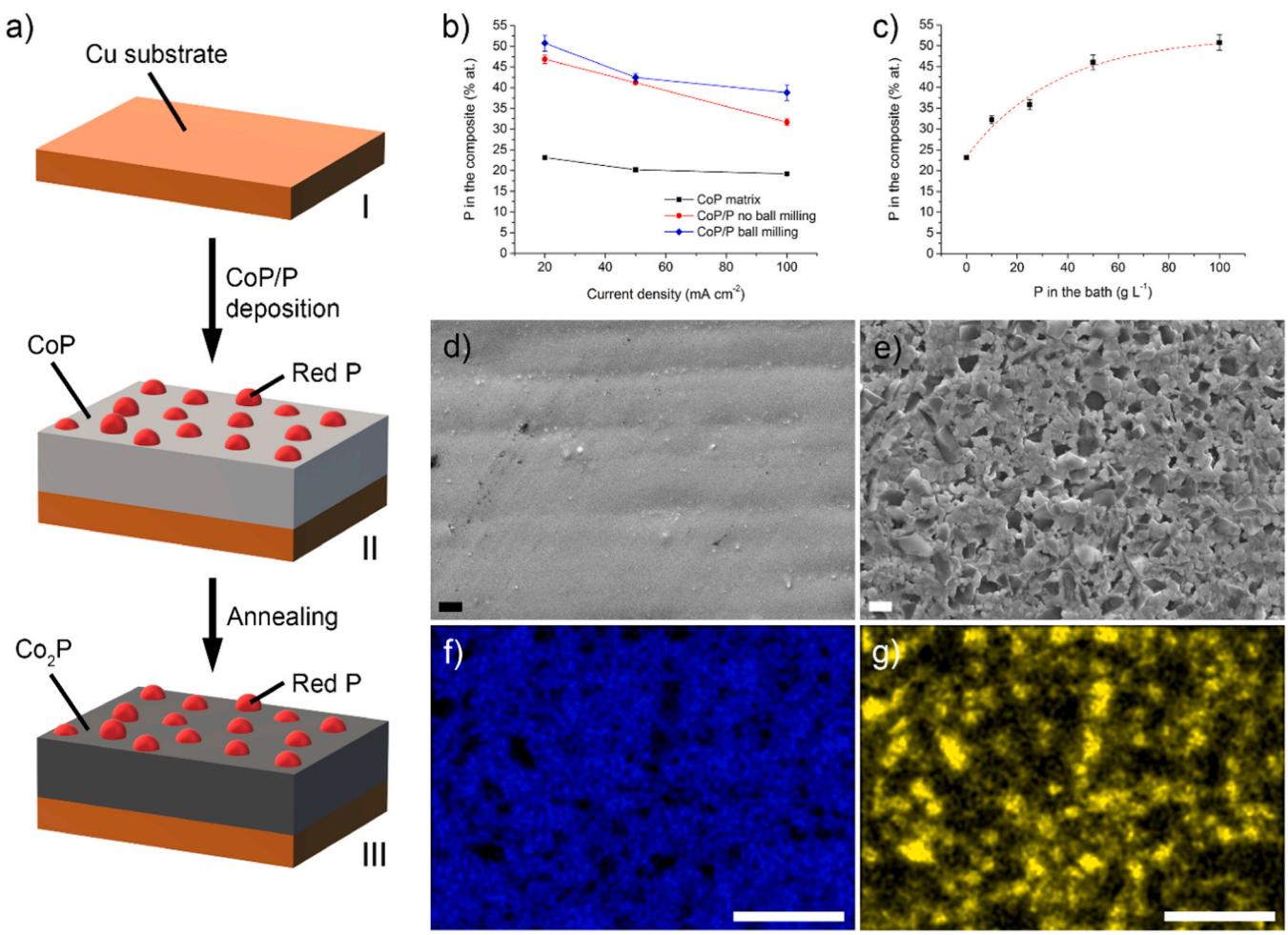

Fig. 1. Manufacturing route for the Co_2P/P nanocomposite preparation (a); amount of P in the composite vs. current density for different electrolytes (b); amount of P in the composite vs. amount of P in the electrolyte (c); SEM of the Co-P matrix deposited at 20 mA cm^{-2} (d, scale bar = 2 μm); SEM of the Co-P/P composite deposited at 20 mA cm^{-2} (e, scale bar = 2 μm); EDS elemental mapping for Co for the Co-P/P composite deposited at 20 mA cm^{-2} (f, scale bar = 10 μm); EDS elemental mapping for P for the Co-P/P composite deposited at 20 mA cm^{-2} (g, scale bar = 10 μm).

mixed with enough of this solution to reach a volume equal to 20% of the final volume (e.g., in the case of 200 mL of finished electrolyte, enough solution was added to 20 g of red phosphorus to reach 40 mL). Then, a weight of ceramic balls equal to 10 times the weight of the red phosphorus was added and the resulting mixture of solution, phosphorus and balls was divided in two equal parts, which were loaded into a planetary ball-miller. The mixture was ball-milled for 1 hours at 200 rpm. At the end of the process, the mixture was removed, the red P residues were washed from the balls using the remaining solution to reach the final volume. The pH of the electrolytic solution was corrected to 2 with NaOH. The final dispersion of red P was probe sonicated again to disperse P particles and kept under stirring until deposition. The deposition of the composites was carried out in a current range of 20 – 100 mA cm^{-2}, at 80 °C, under vigorous stirring and for 2 hours. At the end of the deposition process, the samples were sonicated in water to remove loosely adherent P particles, washed thoroughly with demineralized water and then dried with N_2. In order to promote the formation of Co_2P from the Co-P solid solution, the composites were heat treated (step III in Fig. 1a). Annealing was performed in a Carbolite tubular oven, in the presence of a Ar protective atmosphere. The temperature was ramped at a 5 °C/min rate and the samples were cooled naturally at the end of the process. The following combinations of time and temperature were applied: 1 hour at 300 °C, 2 hours at 250 °C, 1 hour at 150 °C + 1 hour at 250 °C, 1 hour at 250 °C.

When employed in the electrochemical and/or electrochemical/photocatalytic processes the two electrodes were labelled as CoP/P not annealed (Co-P/P) and CoP/P annealed (Co_2P/P), to make the identification of the two materials simpler and more immediate.

2.2.2. Bismuth oxychloride (BiOCl) preparation

Bismuth oxychloride (BiOCl) was prepared *via* co-precipitation synthesis [43]. 33 mL of a 0.1 M KCl aqueous solution were added dropwise to 55 mL of a 0.1 M $Bi(NO_3)_3 \cdot 5\ H_2O$ aqueous solution containing glacial acetic acid (10 wt%). The obtained suspension was maintained under stirring for 24 h at room temperature. Then, the obtained white powder (*ca.* 1 g) was collected by filtration, washed with ultrapure water up to neutral pH and dried overnight in air.

2.3. Materials Characterizations

2.3.1. Co-P/P and Co_2P/P characterization

Scanning electron microscopy (SEM) was carried out using a Zeiss EVO 50 setup, coupled with an Oxford Instruments model 7060 EDS module. The samples were characterized on their top surface and on their cross-section. The latter was obtained by inglobating the deposited materials into epoxy resin. The resulting block was cut, polished and observed. X-ray diffraction (XRD) was performed using a Philips PW 1830 diffractometer in Bragg-Brentano configuration with Cu Kα radiation (λ = 1.54060 Å). The XRD diffraction peaks were identified by comparison with the reference files from the Inorganic Crystal Structure Database.

2.3.2. BiOCl characterization

BiOCl crystal structure and phase composition were determined by X-ray powder diffraction (XRPD) using a PANanalytical X'Pert PRO diffractometer (Cu Kα = 1.54060 Å) equipped with an X-ray source operating at 40 kV x 40 mA. Before the analysis, the powder was finely ground and spread on an aluminum flat-plate horizontal sample holder. The diffractogram was collected in the 10° - 80° (2θ) range (step of 0.02° 2θ and time for each step in 5–96 s intervals). The XRPD pattern was identified by comparison with the JCPDS files from the International Center for Diffraction Data Powder.

UV–vis diffuse reflectance (UV-DR) spectrum was collected at room temperature in 200–800 nm intervals by a double-beam UV–vis–near-infrared (UV–vis–NIR) scanning spectrophotometer (PerkinElmer Lambda 750 s UV–vis spectrophotometer, PerkinElmer, Waltham, MA) equipped with an integrating sphere assembly to evaluate the light absorbance properties of the sample. The powder sample was finely ground, uniformly pressed in a circular disk (external diameter *ca.* 4 cm), and included in the sample holder. The latter was inserted in a special quartz cuvette and placed on the window of the integrating sphere for reflectance measurement. The spectrum was measured using $BaSO_4$ as a reference. The measured reflectance values (R%) were converted to absorbance (Abs, au) by the Eq. (6)

$$\mathrm{Abs} = \log(1/R/100) \tag{6}$$

Tauc's plot was used to evaluate the band gap energy by Eq. (7):

$$(\alpha h\nu)^{1/2} = A(h\nu - Eg) \tag{7}$$

where α, h, and ν represent the absorption coefficient, Planck constant, and frequency of light, respectively, and Eg represents the band gap.

Specific surface area and porosity were determined through N_2 adsorption/desorption isotherms at -196 °C using an automatic analyser (Micromeritics Tristar II 3020). *Ca.* 1 g of dried powder was outgassed at 150 °C for 4 h under vacuum to remove water and other volatile organic compounds adsorbed on the surface. Specific surface area value was calculated by Brunauer−Emmet−Teller (BET) Eq. (2-parameters,0.05< p/p°< 0.3), considering the cross-sectional area of *ca.* 16.2 Å/molecule$_{N2}$. Pore volume and size distribution (PSD) were determined by the Barrett−Joyner−Halenda (BJH) model from the desorption branch of the collected isotherm in the 0.3−0.95p/p^0 window.

The zero-point charge (ZPC) of BiOCl was determined as reported in the literature [44].

BiOCl morphology and elemental analyses were investigated using a scanning electron microscope operating with a field emission source, model TESCAN S9000G, (Overcoached, Germany) with a source of Schottky type FEG; resolution: 0.7 nm at 15 keV (in In-Beam SE mode) and equipped with EDS Oxford Ultim Max (operated with Aztec software 6.0). The sample was supported on metallic stabs with C tape and then coated with Cr employing an ion-sputtering technique to improve the conductivity of the materials.

2.4. Electrochemical characterization of HER in acidic conditions

The activity of the Co_2P/P composites towards HER was studied in acidic conditions (using a 0.5 M H_2SO_4 solution as the electrolyte). The active material was immersed as working electrode (WE) in the solution and graphite was used as the counter electrode (CE). An Ag/AgCl standard electrode (3 M KCl) was used as reference electrode (RE). Tests were performed at ambient temperature and under vigorous stirring. The potential was varied at a scan rate equal to 2 mV s^{-1}. No Ohmic correction was applied. However, the reference electrode (RE) was kept as close as possible to the WE in order to limit potential drops. To assess its stability over time, the Co_2P/P catalyst was cycled in a 0.5 M H_2SO_4 solution for a predetermined number of cycles. The active material was immersed as working electrode (WE) in the solution, graphite was used as the counter electrode (CE) and Ag/AgCl (3 M KCl) was used as reference electrode (RE).The potential was cycled 200 times between 0 and -1.1 V vs. Ag/AgCl. Each test was performed on at least two samples and the best result is reported. In all the tests, a deviation of more than 6% between a samples and the others was never observed. A standard commercial 20% wt. Pt catalyst was characterized and used as a reference to compare properties of the active materials.

2.5. Diclofenac abatement and H_2 evolution through an electrochemical approach

2.5.1. [DCF]= 5 mg L^{-1}

The electrochemical tests were performed in a three-electrodes single chamber electrochemical cell (total capacity = 100 mL) coupled with an

electrochemical workstation (Autolab PGSTAT204, Metrohm). Pt foil (1 ×1 cm^2) was used as the anode, while Pt foil, CoP/P electrode (1 ×1 cm^2), and Standard Calomel Electrode (SCE) were used as cathodes and reference electrode (RE), respectively. In a typical experiment, *ca.* 60 mL of a DCF aqueous solution (5 mg L^{-1}) was used for the test. A 1 M H_2SO_4 solution was added dropwise up to pH = 1 as a supporting electrolyte. Before each experiment, nitrogen gas was bubbled for cell evacuation. Chronoamperometry tests were performed at different potentials (+0.9 V; +1.23 V and +2 V) for 120 min, during which 2 mL aliquots were taken every 30 min. The collected aliquots were quantitatively analysed by high-performance liquid chromatography coupled with a UV–vis detector (HPLC/UV). The HPLC instrument (Agilent 1100 Series) was equipped with a C18 Supelco column (25 cm × 4 mm, 5μm) and a 20 μL injection loop. The chromatographic analyses were performed by an isocratic elution of a mobile phase composed of 50% water, 50% acetonitrile, and 0.1% formic acid at a flow rate of 1 mL/min. The DCF abatement and the related transformation products were monitored at 276 and 260 nm, respectively. The DCF abatement (%) was calculated according to Eq. (8):

$$\text{DCF abatement}(\%) = \frac{C_0 - C_t}{C_0} x100\% \quad (8)$$

where C_0 is the initial DCF concentration, and C_t is the DCF concentration at the analysed time t.

H_2 evolution was quantified when a constant potential of + 2 V was applied between the Pt anode and the RE. Every 60 min, gas samples were collected and analysed by a gas chromatograph equipped with a TCD detector (GC/TCD) instrument. The GC instrument (Hawlett Packard 5890 series II), was equipped with a hp-PLOT Q (Divinylbenzene/Styrene porous polymer) column (30 m x 0.53 mm×40.0 μm Film Thickness), a 500 μL injection loop, and a Thermal Conductivity Detector (TCD). Chromatographic analyses were performed using nitrogen as a carrier gas with a flow rate of 0.7 mL min− 1, oven temperature of 35 °C, injector temperature of 200 °C, and detector temperature of 230 °C.

In some cases, the electrochemical tests were repeated covering the external side of the Pt foil in order to operate with 1 cm^2 surface.

2.5.2. [DCF]= 200 mg L^{-1}

The DCF (200 mg L^{-1}) electrochemical test was performed under the same setup and conditions reported above for the tests carried out using a DCF solution at5 mg L^{-1}. However, because of the low solubility of DCF in an acidic environment, when the drug is present in large amounts ([DCF] > 5 mg L^{-1}), NaOH (1 M) was used as a supporting electrolyte instead of H_2SO_4, increasing the pH of the solution up to 8. The alkaline conditions lead to the drug salification enhancing its solubility in water. As previously described, nitrogen gas was bubbled before each experiment for cell evacuation. Chronoamperometry tests were performed at fixed potential of + 2 V for 120 min during which 2 mL aliquots were taken every 30 min. A high-performance liquid chromatography/UV (HPLC/UV) instrument quantitatively analyzed the collected aliquots. HPLC methods and DCF abatement (%) were the same as defined previously, as well as the H_2 evolution measurement.

In this case, the percentage of organic matter abatement at the end of the EC was measured through chemical oxygen demand (COD) analyses using a COD analyzer (Hach, DR 1900) equipped with a COD analysis kit (Hach, LCK 114). The percentage of organic matter abatement was determined according to Eq. (9)

$$\text{Percentage of organic matter abatement}(\%) = \frac{COD_0 - COD_f}{COD_0} x100\% \quad (9)$$

where COD_0 is the initial COD concentration, and COD_f is the final one after 120 min of electrochemical treatment.

2.6. Electrochemical treatment coupled with Photocatalysis (ECP) for H_2 evolution and diclofenac abatement

In this type of investigation, EC (first step) was coupled with a photocatalytic process (P, second step) to complete the DCF abatement and reduce the COD.

The EC step was performed in the same setup and under the conditions described above (DCF 200 mg/L EC), working at a fixed potential of + 2 V.

Concerning the subsequent photocatalytic process, the resulting waste solution was transferred in a 150 mL glass reactor after the first EC step, and BiOCl (0.5 g L^{-1}) was added. The reactor was inserted into a homemade box with dark walls made of cloth, and the mixtures were allowed to reach adsorption–desorption equilibrium for 30 min in the dark for 30 min. Then, a solar lamp (ULTRA VITALUX 300 W-OSRAM, power density of irradiation of 35 W/m^2 in the UV range and of 49000 lux in the visible range, measured by photoradiometer HD2102.2 Delta Ohm), installed on the top of the reactor at a fixed height (25 cm), was switched on for 180 min. The DCF abatement was monitored for a total time of 210 min, sampling 2 mL aliquots every 15 min for the first 30 min and then every 30 min for the remaining 180 min. The collected samples were placed in 1.5 mL conical vials and centrifuged with a LaboGene ScanSpeed centrifuge at 13,500 rpm for 5 min before any analyses. The collected aliquots were quantitatively analysed through HPLC using the same procedure reported in the previous section.

The percentage of organic matter abatement at the end of the coupled EOP process was performed as reported above.

3. Results and discussion

3.1. Materials preparation and characterization

3.1.1. Electrochemical system: production and characterization of the Co_2P/P electrocatalyst

The first material developed to build the diclofenac degradation electrochemical setup was the Co_2P/P nanocomposite, synthesized by thermally treating the Co-P/P composite, used to catalyze hydrogen production. Given the assumptions of exploiting the HER properties of red P, the first goal for the optimal development of the material was the maximization of P content in the Co-P/P composite itself.

With respect to the methodology developed for Ni-P [20], the present work treats the red P particles dispersed in the bath with the ball-miller. The milling step was found to enhance the codeposition of the red P particles by uniforming their size. Fig. 1b shows the influence of the treatment on the atomic percentage of P incorporated into the final composite (this percentage comprises both the P deposited with Co in the solid solution and the red P codeposited as composite). In order to make a comparison, two additional materials were deposited and characterized via EDS: the Co-P solid solution matrix (without P particles) and the Co-P/P composite obtained without ball-milling (red P was directly dispersed in the electrolyte, without performing ball-milling). In order to maximize the amount of codeposited P, another important parameter is current density. Consequently, all the materials were plated at three different currents to investigate the effect of plating speed on the amount of codeposited P and to identify the best condition.

The first visible effect is the codeposition of higher amounts of red P at low currents. This effect is predicted by the Guglielmi model, which is valid for the electrolytic codeposition of particles in a metallic matrix [45]. According to the model, the amount of codeposited particles is inversely proportional to the current employed. The current not only affects the amount of codeposited red P, but also the amount of P deposited as solid solution with Co [19]. In addition, the ball-milling treatment clearly shows a beneficial effect on the amount of codeposited P, since it crushes larger particles and increases the uniformity of their size distribution. At 20 mA cm^{-2}, for example, the improvement in the amount of red P codeposited was 16.4%.

The Guglielmi model also predicts a dependence of the amount of codeposited red P on the amount dispersed in the bath, and in particular it demonstrates that the amount present in the composite is characterized by a plateau. The maximum amount used in the present work (100 g L^{-1}) basically corresponds to this plateau, as demonstrated in Fig. 1c. In this graph, the concentration of red P dispersed in the electrolytic solution was varied between 0 and 100 g L^{-1}. Consequently, the atomic concentration of P observed at 0 g L^{-1} corresponds to the pure CoP matrix, without red P particles. The presence of the plateau is clearly evident and the exponential fitting performed in Fig. 1c allows to determine that the limit concentration of P obtainable in the composite is 52.3% at. This value is close to the one obtained at 100 g L^{-1} (50.75% at.), demonstrating that further increases in red P concentration in the bath cannot result in significantly higher concentrations in the composite.

Considering the results obtained, the maximum amount of codeposited P was achieved at 20 mA cm^{-2} as plating current and with 100 g L^{-1} as concentration of ball-milled red P particles. These conditions were employed for the production of the composites presented in the following sections of the manuscript. Fig. 1d shows the SEM characterization of the Co-P matrix, without red P particles, plated at 20 mA cm^{-2}, while Figure S1 shows the morphology of the matrix plated at 100 mA cm^{-2}. As expectable in the case of the plating of high P alloys, the morphology is characterized by a very low roughness and by the absence of any visible nodular growth in a wide range of plating currents. The presence of the particles dramatically changes the situation (Fig. 1e). The one depicted in the image is a Co-P/P composite plated at 20 mA cm^{-2}, whose surface roughness is considerably higher if compared to the material reported in Fig. 1d and the red P is clearly visible in the form of particles having maximum diameters around 1 – 1.5 μm. The presence of localized high concentrations of P, corresponding to the microparticles, can be clearly evidenced by observing the EDS elemental mapping for Co (Fig. 1f) and P (Fig. 1g) performed in the same region of Fig. 1e. Figure S2 shows the morphology of the composite deposited at 100 mA cm^{-2}. In this case, the surface looks less rough, probably as a consequence of the lower content of red P.

Once optimized the deposition step, the attention was focused on the heat treatement required to convert the matrix present in the composite into Co_2P. Another important goal for the optimal development of the material was therefore the determination of the optimal combination of annealing time and temperature required to yield a well-formed Co_2P/P nanocomposite.

In general, the Co-P matrix, if exposed to high temperatures, transforms into a mixture of Co_2P and Co. Indeed, the amount of P present in the Co-P solid solution alone (23.14% at.) is not enough to guarantee the formation of stoichiometric Co_2P (which requires 33.33% at.). However, in analogy with was observed in the case of Ni-P [19,20], the red P present in the matrix can diffuse at high temperatures into the matrix and react to form stoichiometric Co_2P. Inevitably, some of the red P is therefore used to supply the excess required for Co_2P formation and cannot be used in its elemental form for HER. However, this is a tradeoff that can be accepted, since also Co_2P is a good HER catalyst.

For what concerns annealing conditions, a first guideline can come from the experience with Ni-P [19,20]. In the case of that system, the formation of a mixture of $Ni_{12}P_5$ and Ni_2P was already observed at 300 °C as annealing temperature and 1 hour as annealing time. Also Co and P are quite reactive and the formation of Co_2P has been observed at temperatures as low as 300 °C [46,47]. However, here the goal is not to completely convert Co and P into Co_2P. On the contrary, some red P should still be present on the surface of the composite after annealing. For this reason, the temperature was varied between a minimum of 250 °C and a maximum of 300 °C, for varying amounts of time. With respect to Ni-P, the phase diagram of Co-P [48,49] is relatively simple. For this reason, the formation of secondary phases is unlike under these conditions. It is also unlike to observe excessive P evaporation, since the vapor pressure of red P is extremely low below 300 °C [19].

Fig. 2a shows the morphology of the composite annealed at 250 °C for 1 h (47.51 ± 1.23% at. P), Fig. 2b that of the composite annealed at 300 °C for 1 h (43.49 ± 0.57% at. P), Figure S3 that of the composite annealed at 150 °C for 1 h + 200 °C for 1 h (46.32 ± 0.45% at. P) and, finally, Figure S4 displays the morphology of the composite annealed at 250 °C for 2 h (45.87 ± 0.88% at. P). If the composition of these annealed samples is compared with the composition of the as-deposited material (50.75% at. P), it appears evident that, despite the low temperatures employed, some of the red P present in the composite evaporated.

Regardless of the temperature and time employed for the annealing, however, the P particles are always present on the surface of the samples. From this point of view, the situation is dissimilar with what observed for Ni-P [19,20]. In the case of Ni-P, the particles completely disappeared and the final material looked uniform, also at 300 °C for 1 h. Under comparable conditions, the particles are still present, but some voids and porosities are visible on the surface (Fig. 2b). Furthermore, if the same sample is observed at higher magnifications (Figure S5), the presence of a gap between the matrix of the composite and the particles appears evident. This is probably the consequence of partial evaporation and diffusion into the matrix.

The considerable difference observed between the Co-P system and the Ni-P system is probably correlated with the different diffusivity of elemental P into the crystal lattice of the forming Co_2P and Ni_2P with respect to the Co-P or Ni-P solid solution. In the case of cobalt, for example, the diffusivity for P is much higher in the Co-P solid solution than the crystalline Co_2P phase [50]. In addition, there is also an intrisic difference between Co_2P and Ni_2P for what concerns the mobility of elemental P [51,52]. It is therefore possible that red P can totally diffuse and react in the case of Ni-P but not in the case of Co-P at 300 °C.

Nevertheless, the formation of a P enriched matrix can be demonstrated by performing EDS on the sections of the composites. Fig. 2c shows the cross-section of the as deposited composite, while Fig. 2e shows the cross section of the composite annealed at 250 °C for 1 h. Figs. 2d and 2f represent the EDS elemental mapping of the same two composites. From the qualitative point of view, the direct comparison of the P signal suggests that some of the elemental P diffused in the matrix. The difference in intensity of the P signal in Fig. 2d looks more accentuated between the particles (zones with high P signal) and the matrix (which contains a smaller amount of P in the form of a solid solution with Co) with respect to Fig. 2f. The latter image shows a more uniform signal across the coating. In order to get more quantitative results, EDS line profiles were acquired from the two samples (Figure S6 for the as plated and Figure S7 for the annealed one). The ratio between the P signal in correspondence with the red P particles and the signal from the matrix was calculated and it resulted equal to 3 for the as plated and 1.81 for the annealed. These values suggest that the difference between particles and matrix in terms of P content is less after annealing.

The presence of a P enriched matrix is not by itself an evidence of the formation of Co_2P. For this reason, XRD was performed to investigate the phase composition of the layers. Prior to annealing, the layers were found to be amorphous (Fig. 3a) regardless of the current employed to deposite them or the P content. Indeed, Co-P solid solutions are amorphous at P contents above 10–12% at., while elemental red P particles are always amorphous. For these reasons, the Co-P/P composite is expected to be amorphous too. The substrate is visible at 50.5° with the Cu (200) peak.

The situation drastically changes if the Co-P/P composite is exposed to heat. Fig. 3b shows the XRD patterns of the composite treated in different ways. Regarding the substrate, the Cu (111) peaks appeared at 43.3°, as a consequence of high temperature recrystallization of copper. For what concerns the active material, some of the peaks related to the presence of orthorombic Co_2P (ICSD 98–002–5726) are clearly visible in the two samples annealed at 250 °C for 1 h and for 2 h [53]. The peaks observed at 40.7° (112/210), 43.4° (211), 48.2° (013) and 52.4 ° (020) can be attributed to Co_2P formed at 250 °C, in accordance with the

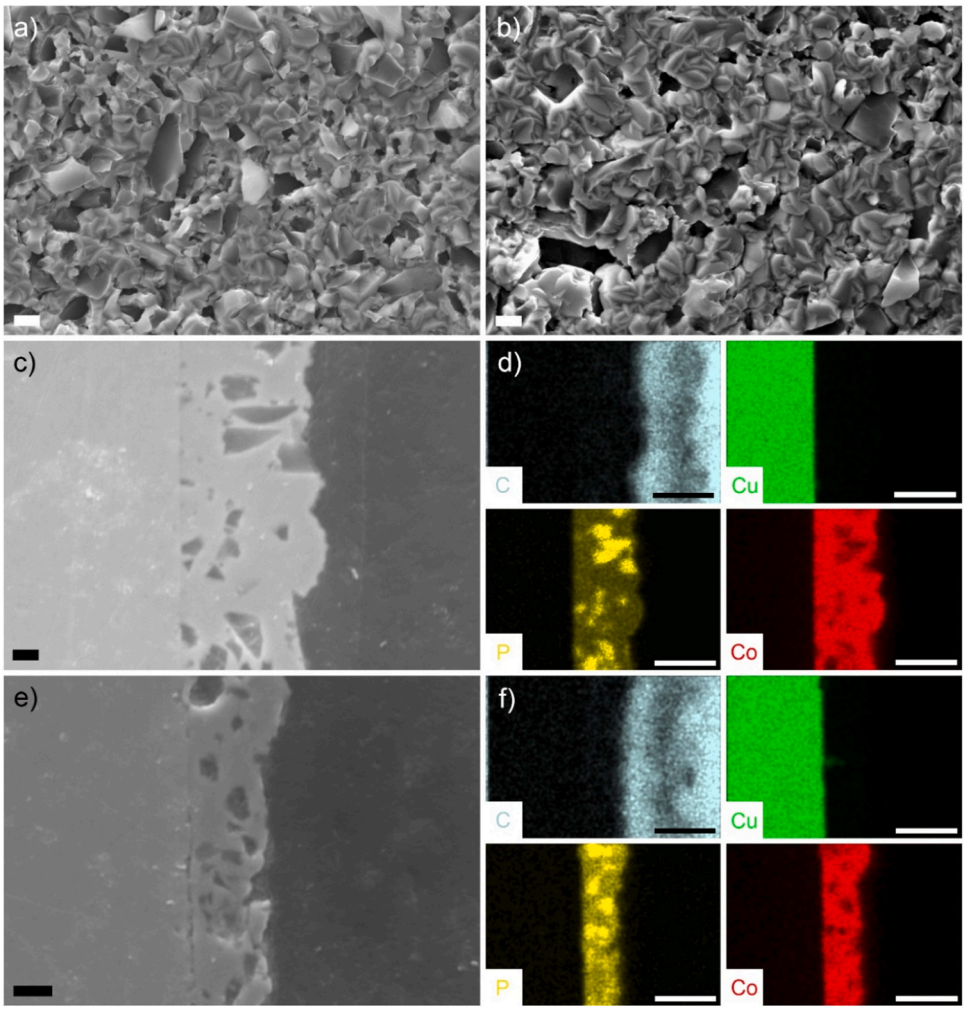

Fig. 2. SEM images of the: composite annealed at 250 °C for 1 h (a, scale bar = 2 μm), composite annealed at 300 °C for 1 h (b, scale bar = 2 μm); cross-section of the as deposited composite (c, scale bar = 2 μm) and of the composite annealed at 250 °C for 1 h (e, scale bar = 3 μm); EDS elemental mapping of the as deposited composite (d, scale bar = 10 μm) and of the composite annealed at 250 °C for 1 h (f, scale bar = 10 μm).

literature, [54], confirming the transition from the Co-P/P composite to the Co_2P/P composite.

In the case of the two samples annealed at 1 h 150 °C + 1 h 250 °C and 300 °C, the XRD graph confirms the presence of Co_2P but it also demonstrates the formation of Cu_3P in correspondence of the interface between the composite and the substrate. The six peaks observed at 36°, 39.1°, 41.5°, 45.1°, 46.2° and 47.3° are indicative of the formation of hexagonal Cu_3P, which results from the reaction between Cu and the red P diffusing out of the red P particles and the P present in the solid solution. The formation of this compound, whose presence is realistically confined to the region close to the substrate, occurred only for the longest anneling duration and at the highest anneling temperature. Cu_3P is in turn a good HER catalyst [55], but do to its localization at the Co-P/P interface with Cu its contribution was not expected to be significant.

The XRD analysis confirmed the presence of a Co_2P matrix with residual red P for all the samples, with the samples annealed at 250 °C presenting the most interesting phase composition. Starting from this result, the HER performances of the materials were tested in acidic conditions in order to determine which presented the best kinetics. A typical 0.5 M sulfuric acid solution was used for the tests and, toghether with the samples obtained at the four annealing conditions previously mentioned, also the following materials were characterized for comparison: the pure copper substrate, the Co-P/P composite before any annealing process and a 20% wt. standard Pt catalyst. The results obtained are reported in Fig. 3c. As expectable, the Pt catalyst presented the lowest overpotential for HER evolution at the reference current of 10 mA cm^{-2}: 35.6 mV vs. RHE. The Cu substrate, being copper a poor electrocatalyst, was characterized by the largest overpotential (η_{10} = 496.8 mV vs. RHE). For what concerns the active material, its HER activity was found to be greatly dependent on the annealing conditions. Table 1 reports the overpotentials recorded for the different samples.

The as-plated material presented limited HER performances, while the annealed ones were characterized by considerably better performances. A clear dependance on anneling conditions was observed, with the samples annealed at higher temperatures or higher annealing durations typically presenting the highest overpotentials. The potential reasons behind this behavior can be the formation of oxides (from oxygen impurities present in the Ar atmosphere), the lower concentration of P resulting from partial evaporation or the local depletion of P in correspondence of the first surface layers. The latter contribution, observed in the case of Ni-P [19,20], may have a predominant effect on the determination of the final performances (Table 1). In order to evaluate the kinetic properties of the materials, the acquired potential-current curves were plotted in the form of Tafel plots (Fig. 3d). Then, the Tafel slopes were evaluated (Table 1). All the annealed materials presented slopes significantly lower than non annealed Co-P/P (125.3 mV dec^{-1}) and Cu (135.4 mV dec^{-1}). The characterization of the Co_2P/P composite was completed by evaluating its stability over time for HER. The tests carried out on the composite annealed at 250 °C for

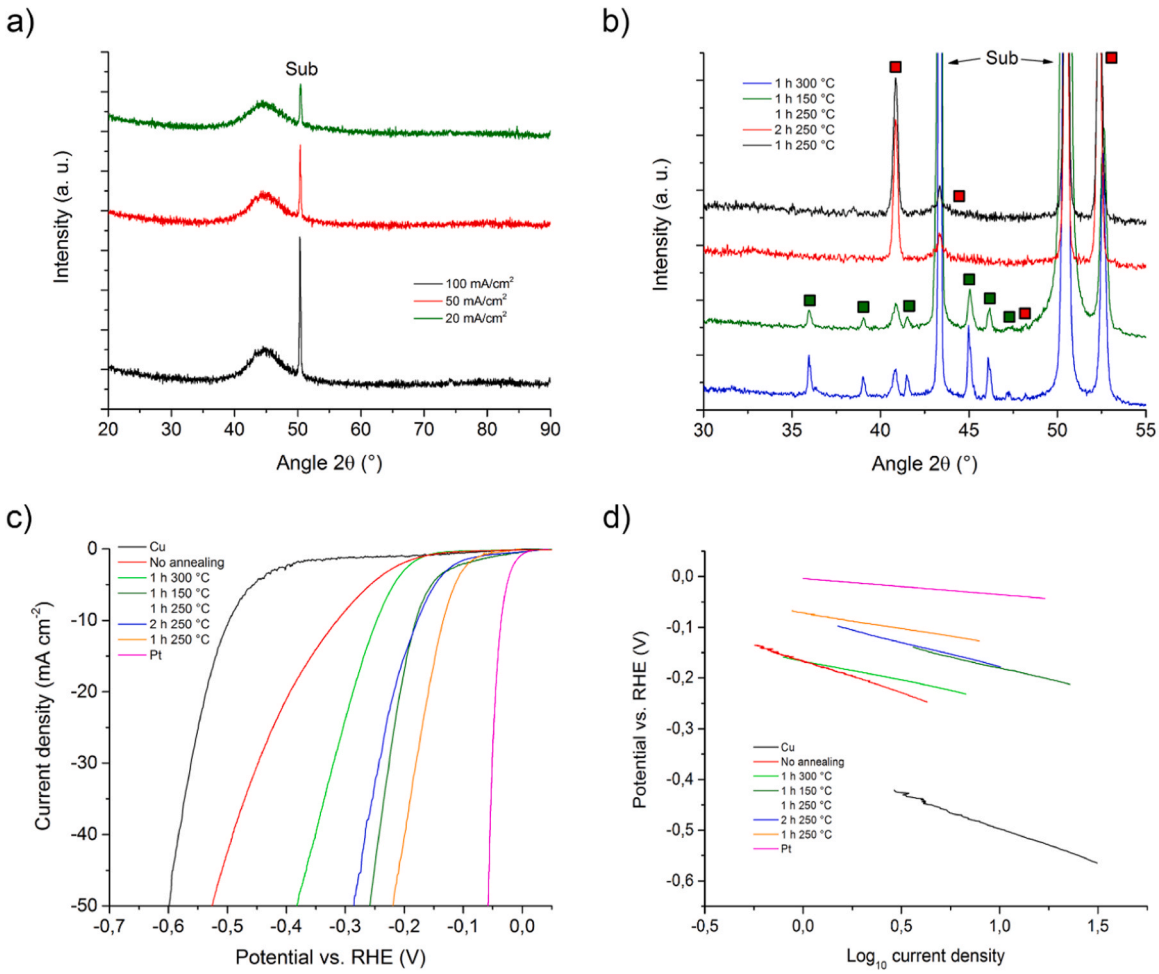

Fig. 3. XRD characterization of the as-deposited Co-P/P composites (a); XRD characterization of the Co2P/P composites formed after annealing (b); linear polarization tests performed in 0.5 H_2SO_4 on the different materials (c); Tafel plots obtained from the linear polarization tests carried out on the different materials (d).

Table 1
HER parameters for the tested materials.

	η_{10} (mV vs. RHE)	Tafel slope (mV dec^{-1})
Cu substrate	496.8	135.4
Co-P/P no annealing	313.8	125.3
1 h 300 °C	246.3	76.4
1 h 150 °C + 1 h 250 °C	179.7	89.1
2 h 250 °C	176.9	94.7
1 h 250 °C	133.6	60.5
Pt 20% wt.	35.6	32.0

1 h evidenced a limited variation of the η_{10} value after 200 cycles (figure S8). The initial value was equal to 136.2 mV and the final one to 143.3 mV, indicating a 5.2% increase.

From the morphological point of view, the SEM analysis carried out on the post-HER sample evidenced the formation of a network of cracks (figure S9), which didn't compromise the structural stability of the material. The EDS analysis evidenced that the cycled surface was characterized by the presence of an oxygen content between 3% and 4% at., whereas the oxygen concentration prior to the test was almost negligible. On the other hand, the ratio Co/P was found to be nearly stable (1.105 before the test, 1.121 after the test). However, if on one hand the cracks formation does not compromise the material activity in standard conditions, in the conditions used for DCF oxidation/H_2 production (in both acidic and alkaline environments) a lower material's stability was experienced (as described below), that could be attributed to a gradual penetration of DCF and its metabolites through the cracks.

Considering both the η_{10} and the Tafel slope, the best material was the Co_2P/P composite obtained at 1 h as annealing time and 250 °C as temperature. This composite, which is characterized by a η_{10} equal to 133.6 mV and a slope of 60.5 mV dec^{-1}, represents the best choice for the construction of the diclofenac electroxidation setup. In general, if compared with some significant examples of HER cataysts based on Co and P (Table 2) reported in the literature, the material sinthesized in the present work presents interesting HER performances.

In general, the performances of the material here described are lower than CoP-rich materials. This is expectable, since the activity of CoP is higher than Co_2P [14] and most of the material here described is constituted of Co_2P. On the contrary, our electrocatalyst competes well with Co_2P containing materials, despite their nanostructured morphology. These comparatively good performances can be realistically justified by the presence of elemental red P particles in the composite, which is a good HER catalyst itself. Consequently, its presence may enhance the activity of the composite layer despite the non nanostructured morphology of our material. Co_2P/P also compares well with respect to electrodeposited Co-P films operated as HER catalysts under acidic conditions.

3.1.2. *Photocatalytic system: BiOCl photocatalyst characterization*

For the final degradation of the selected organic pollutant (DCF) BiOCl was selected for his high photocatalytic activity [41,42], synthesized by a common coprecipitation reaction and properly characterized, as described below.

Table 2
Relevant literature references for HER catalysts based on Co and P.

Cobalt phosphide form	Manufacturing method	Loading (mg cm^{-2})	Electrolyte	η_{10} (mV)	Tafel slope (mV dec^{-1}	Ref.
CoP nanoparticles	Solvothermal synthesis	2	0.5 M H_2SO_4	75	50	[56]
CoP branched nanostructures	Solvothermal synthesis	1	0.5 M H_2SO_4	100	48	[57]
CoP/Co_2P@PC	Complex calcination	1	0.5 M H_2SO_4	72	49	[58]
CoP@CC	Solvothermal synthesis	0.92	0.5 M H_2SO_4	67	51	[59]
Co_2P/CoP NPs	Precursors calcination	0.2	0.5 M H_2SO_4	160	56	[60]
Co_2P nanorods	Solvothermal synthesis	1	0.5 M H_2SO_4	134	-	[61]
Co-P	Electrodeposition	-	0.5 M H_2SO_4	148	74	[62]
Activated Co-P	Electrodeposition	-	1.0 M KOH	85	37	[63]
Co-P	Electrodeposition	-	1.0 M KOH	94	45	[64]
Co-P/P composite	Electrodeposition	3.32	0.5 M H_2SO_4	133.6	60.5	This work

The crystal structure and phase composition of BiOCl were investigated by x-ray powder diffraction, and the result is displayed in Figure S10.

The sharp peaks indicate that BiOCl is characterized by a good crystal quality. All the main diffraction peaks correspond to the tetragonal structure of BiOCl with a space group of P4/nmm (JCPDS, 85–0861) [65]. Other than the BiOCl peaks, no others were observed, indicating the high purity of the material. Compared with the reference diffraction pattern (JCPDS, 85–0861), the intensity of the diffraction peak corresponding to the (110) plane is stronger than that of other planes. According to the literature, this can be attributed to a preferential growth orientation of the crystals along the (110) plane during the synthesis [66]. As demonstrated by Yang *et al.* [41], the preferential exposition of the (110) crystal plane enhances the migration of holes and reduces the recombination of photogenerated electron–hole pairs, ensuring high photocatalytic performances even under solar light irradiation.

In order to investigate morphology, topography, and elemental composition of the synthesized BiOCl more in-depth, FESEM and Energy-Dispersive X-ray Spectroscopy (EDS) analyses have been carried out: the main results are reported in Figs. 4 and 5.

Fig. 4 shows that BiOCl comprises flower-like micrometric aggregates; see section a (medium-magnified image). If the BiOCl' flowers" are inspected at higher magnification, it is possible to single out the individual 'petals' that constitute the different aggregates: in both b and c sections, there are indications of either a lesser (section b) or a more challenging agglomeration grade. Moreover, the tiny thickness of the layers is clearly observable and if measured, it falls in the 15–30 nm dimensions range.

In order to assess the elemental composition of the investigated material, EDS analysis was carried out: the relevant spectrum is reported in section a of Fig. 5: all the expected elements are present, besides C, which is reminiscent of the carbon tape employed to run the electron microscopy measurements. In the mapping reported in section b of Fig. 5, the elemental analysis also evidences a good contact among Bi, O, and Cl species, confirming the location of the elements in each other.

Concerning photocatalysts characterization, investigating the point of zero charge (pH_{pzc}) is crucial to understanding the molecule-photocatalyst interaction [67]. Figure S10b) shows the results obtained for the synthesized BiOCl.

The pH_{pzc} of BiOCl was 4.46. It is worth noting that different factors affect the pH_{pzc} of the materials (*e.g.*, chemical/physical characteristics of the sample surface, pH medium, *etc.*), [67]. This parameter provides information about the type of charges prevailing at the material surface that are pH-dependent. In fact, positive charges prevail for pH values below the pH_{pzc}, leading to anionic species' attraction. In contrast, for pH values above pH_{pzc}, the material's surface is negatively charged, thus attracting cations.

The band gap and the optical absorbance characteristics of the synthesized photocatalyst were investigated through UV–visible diffuse reflectance spectroscopy (DRS), as shown in Figure S10 c) and d).

The DRS spectrum (Figure S10 c) shows that the absorption edge of BiOCl is about 360 nm, according to what is reported in the literature [68]. The band gap energy of BiOCl was calculated by Eq. 7, where n is determined by the type of optical transition of a semiconductor, that is 4 for BiOCl. Therefore, E_g was 3.35 eV.

3.2. Diclofenac abatement and H_2 evolution though EC approach

Conventionally, noble metals-electrodes are employed for water electrolysis [69,70]. Although, in general, Pt-based electrodes show superior activity, they are too expensive to be used on a large scale. Therefore, developing innovative cheap materials is a crucial aspect for real applications. Based on these premises, the present work is focused on developing alternative, cost-effective noble metals-free electrodes able to replace traditional Pt electrodes at the cathode to maximize the

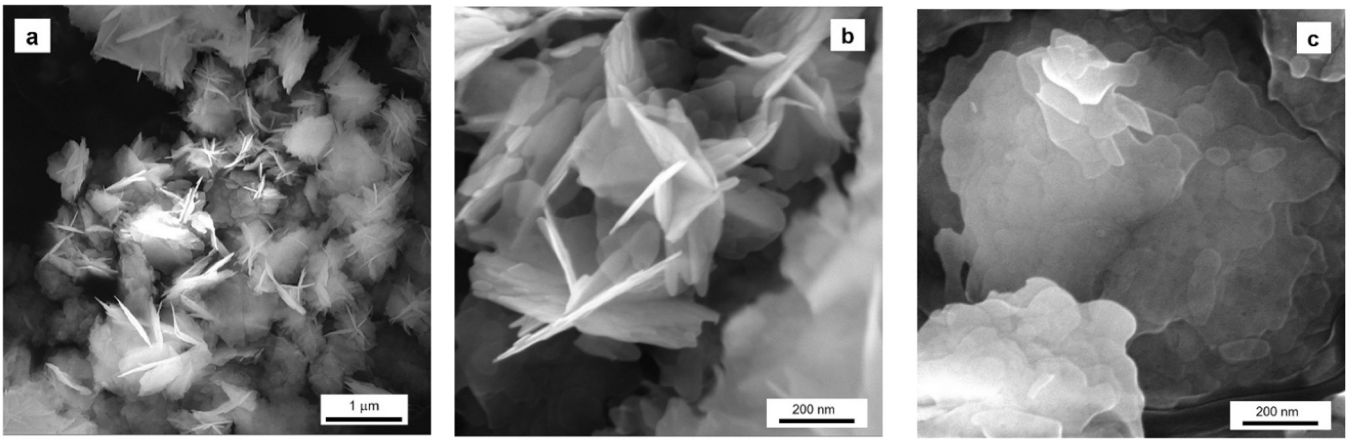

Fig. 4. FESEM images of BiOCl. Section a: medium magnification; sections b and c: high magnification.

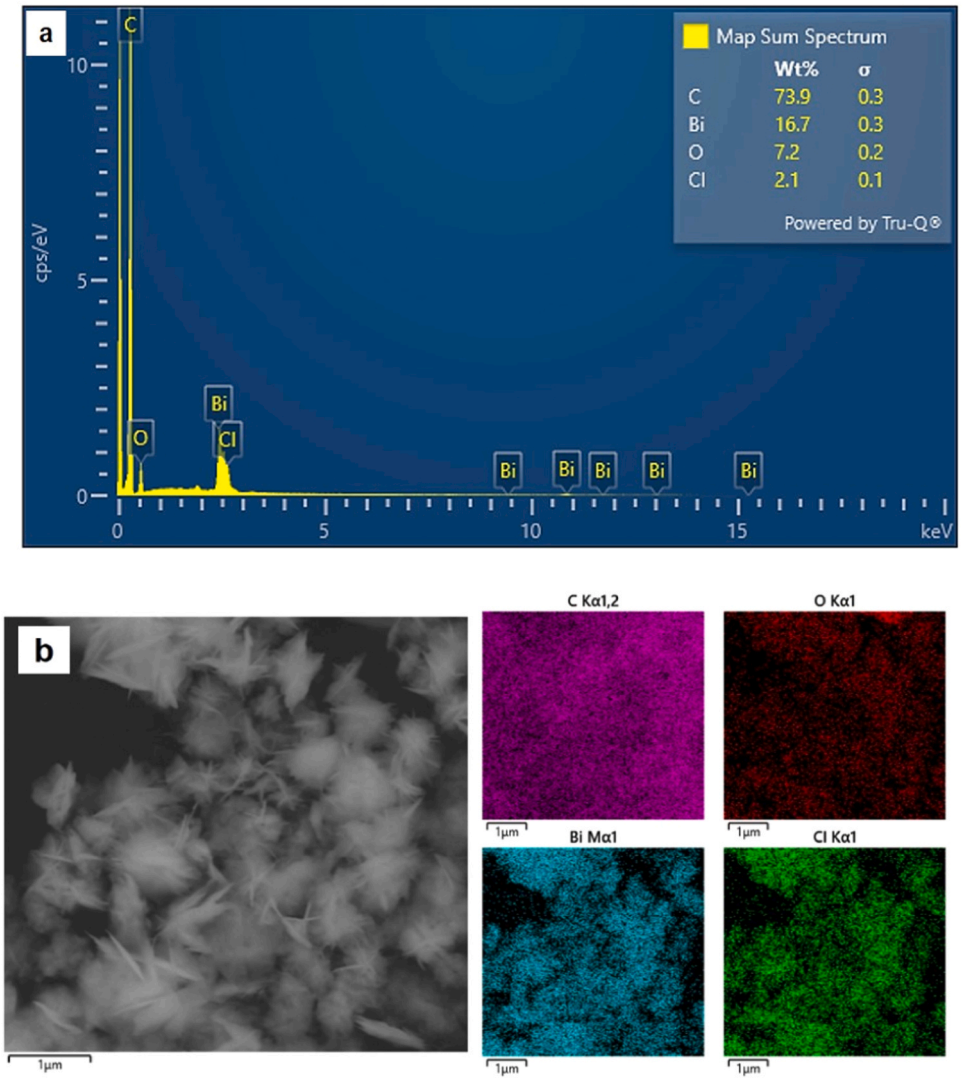

Fig. 5. Section a: EDS spectrum of BiOCl; section b: elemental mapping of the same region reported in Fig. 4, section a.

H_2 evolution during the electro-oxidation of organic components (DCF as model molecule). The CoP/P electrodes described above were tested in combination with Pt electrode at the anode (as standard electrode) for the simultaneous H_2 evolution and abatement of the organic components (DCF) in different conditions. Moreover, the performances of the CoP/P electrodes were compared with those of a traditional Pt electrode, and the results are discussed below.

The Pt electrode was selected for its high stability and well-known characteristic, to investigate the behaviour of the innovative cathode selectively [71–73].

The flow diagram of the EOP process is illustrated in Figure S11.

At first, the simultaneous DCF abatement and H_2 evolution process was investigated in an acidic environment (pH 1), maintaining the drug concentration at 5 mg L^{-1} because of its low solubility. The effect of bias potential (from +0.9 to +2 V) on DCF degradation and H_2 production was investigated for both the synthesized cathode materials (Co-P/P annealed and Co-P/P not annealed) and for Pt foil as reference (Fig. 6). Preliminary investigations indicated that, while DCF electro-oxidation was observed even at lower potentials (*i.e.,* +0.9 V and +1.23 V), no H_2 evolution was detected in these conditions due to the insufficient electrical potential registered in the cathodic section (*c.a.* -0.3 V).

The DCF degradation is observed at all applied bias potentials, regardless of the type of material used for the counter electrode. The percentage of DCF removed and the degradation rate increase with the increase of the applied bias potential. In general, for bias potentials of +0.9 and +1.23 V, the use of Pt foil or CoP/P annealed as cathode leads to low DCF abatement (25% for Pt cathode and 35% for Co-P/P annealed cathode), increasing for higher values of applied bias potentials (+2 V), achieving a percentage of DCF degradation of 70–80%. In contrast, when Co-P/P not annealed is used as the cathode, the DCF degradation rate is superior in all the explored conditions, reaching a percentage of DCF abatement greater than 70% already at +1.23 V. On the other hand, as reported in the literature [14], the performances of CoP -based materials are higher than those of Co_2P-based ones. During the electrochemical process, if on the one hand the Pt foil and the Co-P/P not annealed did not show evident modification, on the other hand the Co-P/P annealed cathode underwent a gradual deterioration. Recently, Zhao *et al.* [74] described the two possible mechanisms responsible for the DCF degradation: direct oxidation and indirect oxidation mediated by reactive oxidants (ROs) generated during the electrolysis of H_2O [75].

The hydrogen evolution rate was evaluated for the tests carried out at an applied bias potential of +2 V (Fig. 6d). It is evident that the Co-P/P annealed electrode, in conformity with the data obtained during the electrocatalytic characterization (Fig. 3c and Table 1), obtains a more significant H_2 amount. The investigations demonstrated that the current density of Co-P/P-based electrodes is higher than that recorded for the Pt foil reference (Table 3).

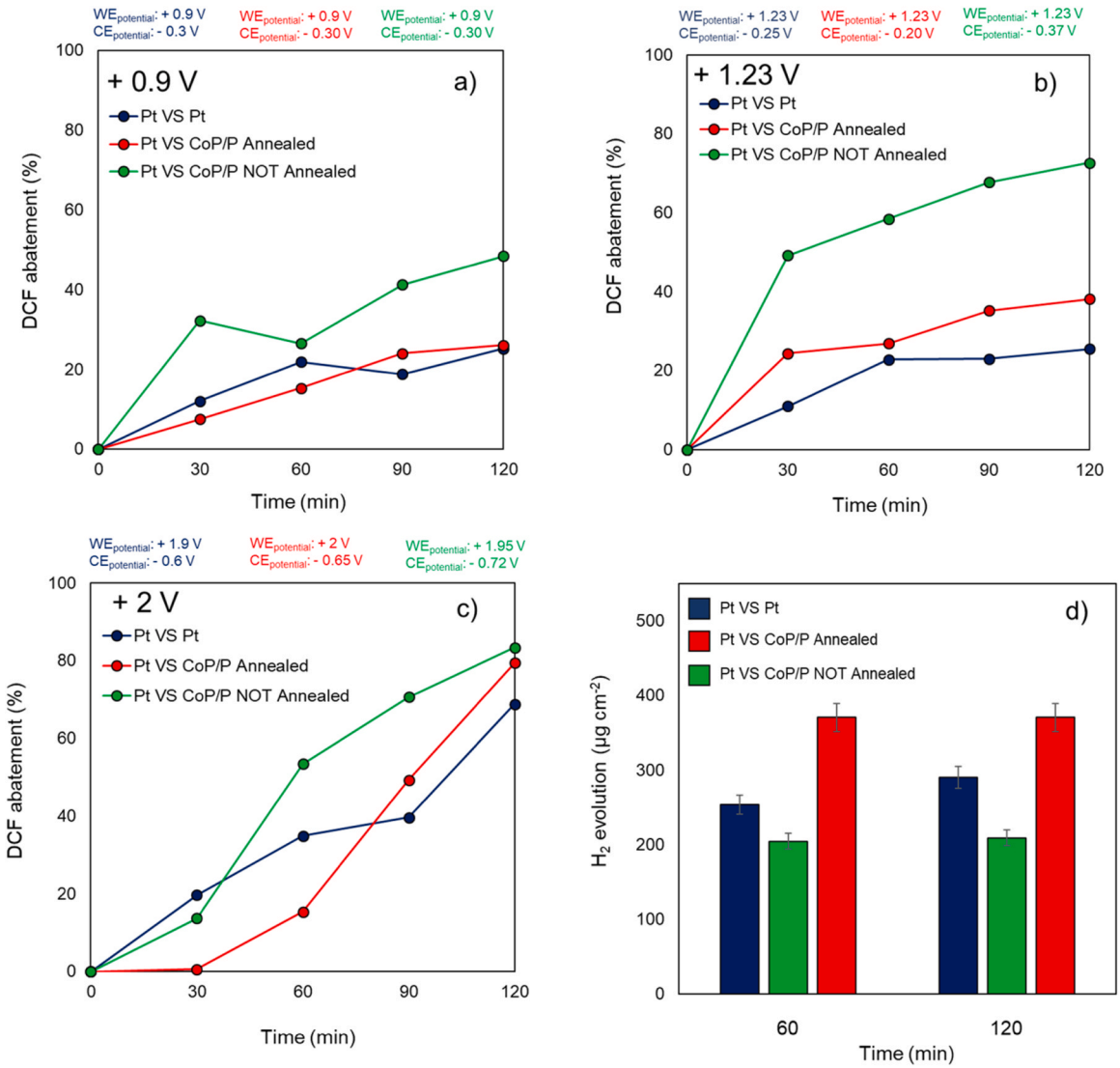

Fig. 6. a-c) Effect of applied bias potential on DCF abatement and d) H_2 evolution quantification in the presence of Pt, Co-P/P annealed, and Co-P/P not annealed cathode (Pt anode) in acidic conditions ([DCF] = 5 mg/L) applied potential +2 V.

Table 3
Current density developed during DCF degradation at +2 V of applied bias potential and power consumed by the electrodes.

Cathode material	pH and drug conc.	Current density (µA/cm^2)	Power (µW)
Pt foil	pH 1, DCF 5 mg/L	20.0	40.0
CoP/P annealed	pH 1, DCF 5 mg/L	40.2*	80.4
CoP/P not annealed	pH 1, DCF 5 mg/L	40.3	80.6
Pt foil	pH 8, DCF 200 mg/L	9.8	19.6
CoP/P annealed	pH 8, DCF 200 mg/L	20.2**	40.4
CoP/P not annealed	pH 8, DCF 200 mg/L	20.6	41.2

* The value is not stable during the experiment.
** The value quickly goes to zero during the test.

The values of power consumed by the electrodes was calculated by Eq. (10)

$$Power(P) = I * V \quad (10)$$

However, although both the Co-P/P-based materials exhibit higher current density values than Pt foil, thanks to their greater stability in the explored conditions, only Co-P/P not annealed displayed the most interesting performances.

In Fig. 6a Pt foil (1 cm per side) was used as electrode. However, for comparison, test at +2 V were repeated covering the side of each electrode opposite respect that of the other (Fig. S12). However, the intensity of the electric field is considerably higher on the face of the Pt foil placed in front of the cathode with respect to the opposite one. Due the relative position between the electrodes, it is expectable to see current densities that are orders of magnitude different on the two faces. Consequently, the use of a double side Pt electrode does not significantly alter the measurement, as displayed in Fig. S13.

The electrochemical behavior of the synthesized cathode materials was investigated in the presence of a larger amount of pollutants. In this regard, to increase the DCF concentration in an aqueous solution, it was necessary to increase the pH of the solution up to 8. In this manner, a 200 mg/L DCF solution was obtained for the electrochemical process using an applied bias potential of +2 V.

Fig. 7 summarises the obtained results.

As observed in acidic conditions, also in alkaline conditions and with a DCF concentration forty times greater, the presence of Co-P/P not annealed as cathode leads to a higher DCF abatement (ca. 70%),

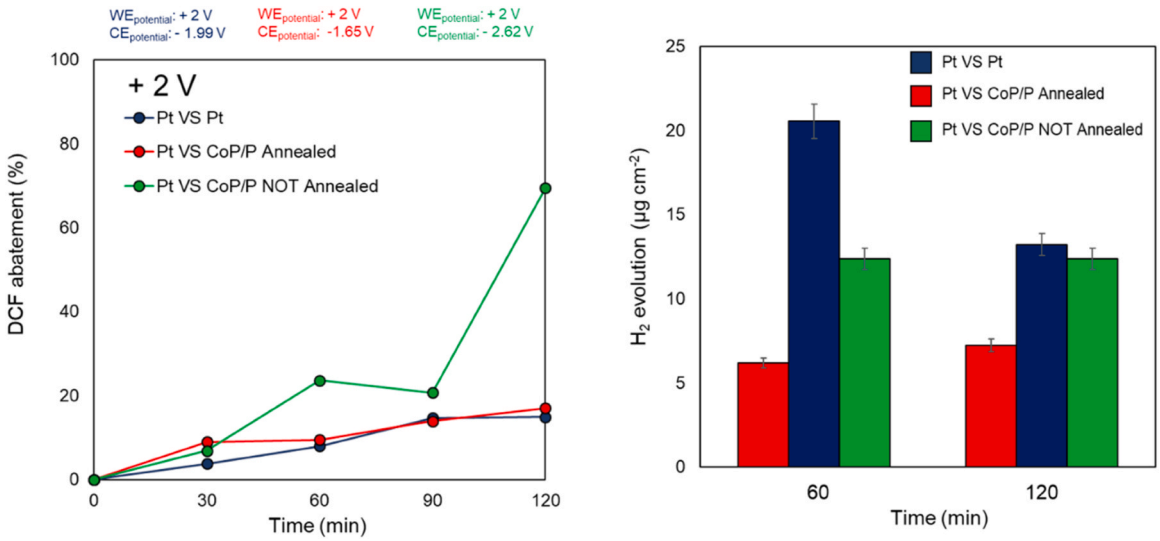

Fig. 7. a) DCF abatement and b) H_2 evolution quantification in the presence of Pt, Co-P/P annealed, and Co-P/P not annealed cathode (Pt anode) in alkaline conditions ([DCF] = 200 mg/L) at +2 V of applied bias potential.

whereas for Pt foil and Co-P/P annealed it remains lower than 20%. The evaluation of the current density developed is reported in Table 1, showing that Co-P/P-based cathode materials exhibit double-digit values compared to the Pt foil. Also, in this case, the low stability of Co-P/P annealed causes a fast and drastic decrease of both current density value and electrochemical performances during the test, justifying the low performance of the entire cell towards DCF degradation.

However, despite the high percentage of DCF degradation obtained by coupling the Pt foil anode with the Co-P/P not annealed cathode, the percentage of organic matter abatement was low (16%), comparable to the results achieved by the Pt-Pt cell. The analyses performed on the treated solutions did not allow for the identification of the degradation products responsible for this effect, probably related to the presence of small species with low molecular weight requiring the use of different analytical techniques, such as ion chromatography, to be detected and identified.

Concerning the hydrogen evolution rate (Fig. 7b), in contrast to what was previously observed in acidic conditions, the Pt foil electrode leads to the greatest H_2 amount at the beginning of the treatment. However, it quickly decreases, matching those of the Co-P/P not annealed material. The deterioration of the Pt foil features could be associated with poisoning of the electrode surface caused by specific by-products produced during the DCF degradation. In contrast, the Co-P/P not annealed cathode material maintains high stability during the EC process, exhibiting a constant value of H_2 evolution.

Fig. 8 summarizes the mechanism of DCF abatement both in acid and alkaline environment.

In acidic environment, the main reaction the reactions described in Eqs. 2 and 3 take please is [72]:

OH·(Eq. 3) can undergo a subsequent oxidation step producing atomic radical oxygen through Eq. 11:

$$OH\bullet \leftrightarrow \bullet O\bullet + e^- + H^+ \quad (11)$$

Both hydroxyl and atomic oxygen radicals can act as oxidizing agent for the organic species present in solution but the former is the most reactive. In addition, ·O· can combine with another atomic radical oxygen (·O·) leading to O_2. DCF oxidation by direct electron transfer can also take place but its contribution is smaller compared to the generation of reactive radicals [72].

In alkaline conditions, the reactions describe in Eqs. 4 and 5 take place.

At high values of pH the DCF anionic form is the prevalent one and could migrate at the anode, due to concentration difference. to be degraded by OH· and ·O·. Also in this case, as described in the literature [72], direct oxidation can take place in DCF abatement.

3.3. H_2 evolution and diclofenac abatement through EC coupled with Photocatalysis (EOP)

In order to optimize the DCF degradation to complete the water purification process, a further photocatalytic step was added downstream of the EC process, as depicted in Figure S9. The additional

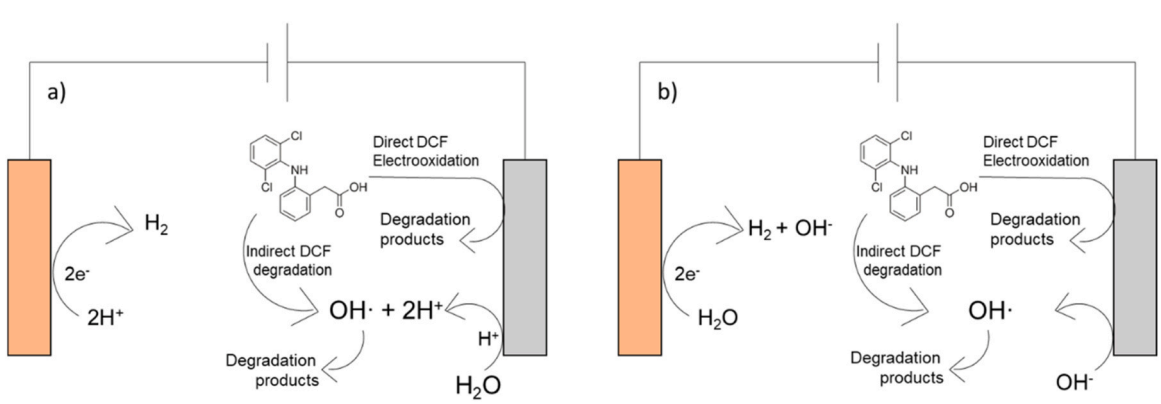

Fig. 8. Mechanism of DCF degradation and H_2 evolution in: a) acidic and b) alkaline environment.

photocatalytic treatment consists of transferring the wastewater, resulting from the EC step carried out using both Pt foil and Co-P/P not annealed cathode materials in alkaline conditions ([DCF] = 200 mg/L) at +2 V of applied bias potential, into a batch reactor equipped with a sunlight source and adding an appropriate quantity of BiOCl as photocatalyst (0.5 g/L). Fig. 9 displays the results obtained in terms of DCF degradation, COD reduction, and monitoring of the main transformation product produced.

Although the band gap value of the synthesized oxide is not suitable to exploit the entire solar electromagnetic spectrum, mainly made up of the visible light, it is able to utilize the UV part effectively, as demonstrated by the photodegradation tests.

It is worth noting that, as discussed above, comparing the percentage of DCF abatement observed when the two different cathodes are used (Pt foil and Co-P/P not annealed), the results obtained by the novel material (Co-P/P not annealed) are more promising, achieving a percentage of DCF removal approximately 4.5 times higher than that of Pt. However, despite these outcomes, the organic compounds abatement capability turned out to be the same. Surprisingly, the addition of the further downstream photocatalytic step leads to different results depending on the cathode material used in the first step. In fact, the combination of the EC-Co-P/P not annealed with the photocatalytic approach permits to achieve the 59% of organic matter abatement, while in the presence of the traditional Pt foil cathode, the first EC step does not improve the organic matter removal process of the drug. Based on these results, it is possible to affirm that, when exposed to large amount of DCF, BiOCl is not able to degrade the drug effectively. It causes the accumulation of a specific transformation product (DCF 259) coming from a dechlorination and ring closure reaction. In contrast, the photocatalyst exhibits high organic matter abatement capacity towards the small molecules produced during the EC process. In fact, although a high reduction of the COD level is obtained when the photocatalytic step follows the EC step executed by Co-P/P, not annealing cathode, the DCF 259 transformation product is produced in a lower amount.

Tables 2 and 4 exhibit a comparison among the performances of different electrodes and those here described in terms of overpotential applied for H_2 evolution reaction and percentage of DCF degraded.

The results show that the materials here investigated exhibit extraordinary activity in terms of DCF removal from water, while in terms of H_2 production Co_2P/P is a good HER catalyst competing with other similar electrodes described in the literature.

4. Conclusion

This study demonstrates the potential of a combined electrochemical and photocatalytic approach for effective wastewater treatment and

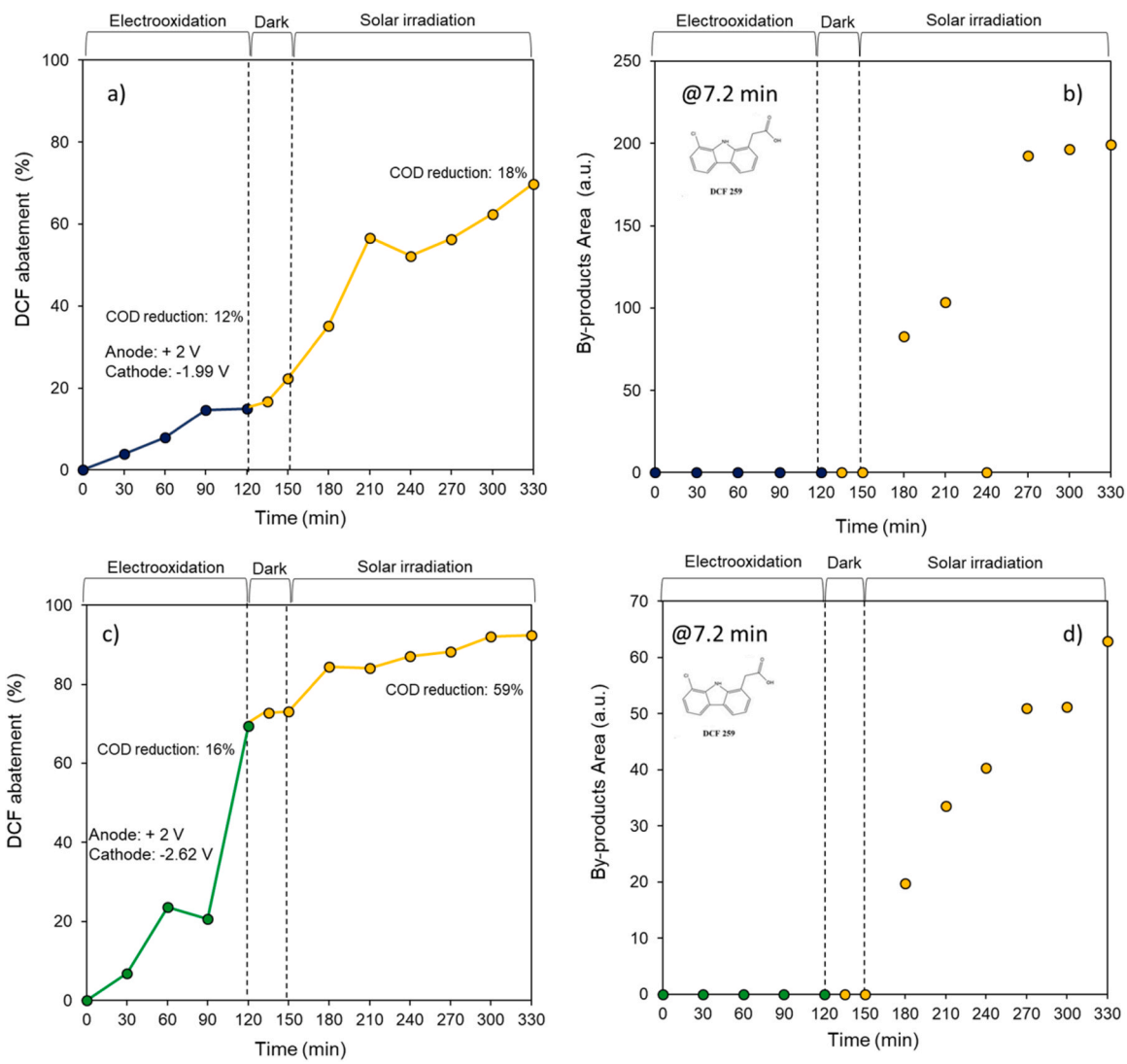

Fig. 9. DCF abatement and COD reduction capacity of the EOP process by the use of Pt foil as anode and a) Pt foil and c) Co-P/P not annealed as cathode; b and d) time-resolved profiles of the main transformation product identified during the photocatalytic step.

Table 4
Comparison of different electrochemical system for DCF electro-oxidation.

Ref.	Working electrode	Electrolyte	Initial DCF concentration (mg/L)	Reaction time (h)	pH	Applied Potential / Current /Charge	% Removal
This work	Pt (1 cm^2)	H_2SO_4 and NaOH	5 (H_2SO_4) 200 (NaOH)	2	1 8	+2 V	80 (H_2SO_4) 70 (NaOH)
[72]	Pt (10 cm^2)	H_2SO_4	80	-	4.5	4200 Coulombs/L	66
[74]	BDD (12 cm^2)	Na_2SO_4	30	4	8.5	+4 V	72
[76]	Carbon brush	Na_2SO_4 Microbe + Fe (Bioelectro-fenton)	0,04	5	2	+0.3 V	97
[77]	Pt-doped SnO2-Sb (20 cm^2)	Na_2SO_4	200	5	-	1 A	91
[78]	BDD on silicium substrate (189 cm^2)	-	10	3	-	0,9 A	100

sustainable hydrogen production. The employment of a noble metal-free Co_2P/P electrode for hydrogen generation through water splitting presents a cost-effective and environmentally friendly alternative to traditional methods. The successful degradation of diclofenac in wastewater using this electrochemical method highlights its efficiency. However, the study finds that electrochemical treatment alone does not achieve complete COD abatement. The incorporation of a subsequent photocatalytic step using BiOCl significantly enhances the removal of contaminants and COD reduction while concurrently sustaining hydrogen production. This integrated approach not only addresses the challenge of energy storage through hydrogen production but also contributes to mitigating the pressing issue of water pollution. Thus, it presents a promising and scalable solution for simultaneously addressing energy and environmental challenges, paving the way for future research and applications in sustainable technology development.

CRediT authorship contribution statement

Alessia Giordana: Formal analysis. **Claudia Letizia Bianchi:** Validation, Supervision, Funding acquisition, Conceptualization. **Luca Magagnin:** Supervision, Data curation. **Iliyan Boykov Iliev:** Formal analysis. **Roberto Bernasconi:** Formal analysis. **Ermelinda Falletta:** Writing – original draft, Data curation. **Eleonora Marcolini:** Methodology. **Vincenzo Fabbrizio:** Formal analysis, Data curation.

Declaration of competing interest

The authors declare that they have no known competing financial interests or personal relationships that could have appeared to influence the work reported in this paper.

Data availability

Data will be made available on request.

Appendix A. Supporting information

Supplementary data associated with this article can be found in the online version at doi:10.1016/j.jece.2024.113139.

References

[1] R.E. Smalley, Future global energy prosperity: the terawatt challenge, MRS Bull. 30 (6) (2005) 412–417, https://doi.org/10.1557/mrs2005.124.
[2] E. Nartowska, et al., Civ. Environ. Eng. Rep. 33 (2023) 39–52, https://doi.org/10.59440/ceer-2023-0003.
[3] A. Arregi, et al., Energy Conv. Manag. 165 (2018) 696–719, https://doi.org/10.1016/j.enconman.2018.03.089.
[4] S. Sharma, et al., Sci. Total Environ. 713 (2020) 136633, https://doi.org/10.1016/j.scitotenv.2020.136633.
[5] W. Zhongyi, et al., Electrochim. Acta 254 (2017) 140–147, https://doi.org/10.1016/j.electacta.2017.09.130.
[6] Y. Zhiping, et al., Appl. Cat. B 160 (161) (2014) 173–178, https://doi.org/10.1016/j.apcatb.2014.05.017.
[7] D. Brown, et al., Electrochim. Acta 29 (11) (1984) 1551–1556, https://doi.org/10.1016/0013-4686(84)85008-2.
[8] M.S. Faber, et al., Electrocatalysis, J. Phys. Chem. C. 118 (37) (2014) 21347–21356, https://doi.org/10.1021/jp506288w.
[9] W.-F. Chen, et al., Chem. Commun. 49 (2013) 8896–8909, https://doi.org/10.1039/C3CC44076A.
[10] F. Wang, et al., Angew. Chem., Int. Ed. 55 (2016) 6919–6924, https://doi.org/10.1002/anie.201602802.
[11] J. Zhang, et al., J. Alloy. Comp. 933 (2023) 167613, https://doi.org/10.1016/j.jallcom.2022.167613.
[12] K. Bhunia, et al., Coord. Chem. Rew. 478 (2023) 214956, https://doi.org/10.1016/j.ccr.2022.214956.
[13] C. Hu, et al., Catalysis 10 (2) (2020) 188, https://doi.org/10.3390/catal10020188.
[14] Y. Pan, et al., J. Mat. Chem. A 4 (2016) 4745–4754, https://doi.org/10.1039/C6TA00575F.
[15] S. Xu, et al., J. Mat. Chem. A 8 (2020) 19729–19745, https://doi.org/10.1039/D0TA05628F.
[16] A. Han, et al., J. Mat. Chem. A 4 (2016) 10195–10202, https://doi.org/10.1039/C6TA02297A.
[17] Q. Cao, et al., Electroanalysis 30 (11) (2018) 2584–2588, https://doi.org/10.1002/elan.201800494.
[18] H. Cao, et al., ChemSusChem 14 (4) (2020) 1094–1102, https://doi.org/10.1002/cssc.202002624.
[19] R. Bernasconi, et al., ACS Appl. En. Mater. 3 (7) (2020) 6525–6535, https://doi.org/10.1021/acsaem.0c00733.
[20] R. Bernasconi, et al., J. Mater. Sci. 57 (2022) 9370–9388. DOI:1007/s10853-022-07251-3.
[21] C. Fung, et al., ACS Chem. Rev. 122 (3) (2022) 3879–3965, https://doi.org/10.1021/acs.chemrev.1c00068.
[22] Y. Zhu, et al., Nanoscale 12 (2020) 13297–13310, https://doi.org/10.1039/D0NR01748E.
[23] L. Xihong, et al., Chem. Soc. Rev. 43 (2014) 7581–7593, https://doi.org/10.1039/C3CS60392J.
[24] S. Murgolo, et al., Water Res. 164 (2019) 114920, https://doi.org/10.1016/j.watres.2019.114920.
[25] A.G. Vlyssides, et al., J. Hazard. Mater. 95 (1-2) (2002) 215–226, https://doi.org/10.1016/S0304-3894(02)00143-7.
[26] X.J. Zhao, et al., Nanoscale 11 (2019) 9319–9326, https://doi.org/10.1039/C9NR02153A.
[27] J. Qiao, et al., J. Water Process Eng. 44 (2021) 102308, https://doi.org/10.1016/j.jwpe.2021.102308.
[28] Reddy K., CRC Press, 2013, 131–147, DOI:10.1201/b15004-14.
[29] S. Feijoo, et al., Chem. Eng. J. 455 (2023) 140627, https://doi.org/10.1016/j.cej.2022.140627.
[30] C. Trellu, et al., Chem. Eng. J. 306 (2016) 588–596, https://doi.org/10.1016/j.cej.2016.07.108.
[31] D. Pęziak-Kowalska, et al., Ecotox. Environ. Safe. 181 (2019) 172–179, https://doi.org/10.1016/j.ecoenv.2019.05.084.
[32] Y. Ouarda, et al., Chemosphere 193 (2018) 160–169, https://doi.org/10.1016/j.chemosphere.2017.11.010.
[33] D. Meroni, et al., Materials 16 (3) (2023) 1304, https://doi.org/10.3390/ma16031304.
[34] D. Ma, et al., Chemosphere 275 (2021) 130104, https://doi.org/10.1016/j.chemosphere.2021.130104.
[35] R. Djellabi, et al., Curr. Opin. Chem. Eng. 33 (2021) 100696, https://doi.org/10.1016/j.coche.2021.100696.
[36] Z. Xing, et al., Appl. Catal. B Environ. 225 (2018) 452–467. DOI:/10.1016/j.apcatb.2017.12.005.
[37] G.N. Shao, et al., Powder Technol. 258 (2014) 99–109, https://doi.org/10.1016/j.powtec.2014.03.024.
[38] M. Skocaj, et al., Radiol. Oncol. 45 (4) (2011) 227–247, https://doi.org/10.2478/v10019-011-0037-0.

[39] G. Zhang, et al., J. Environ. Chem. Eng. 5 (1) (2017) 1196–1204, https://doi.org/10.1016/j.jece.2017.01.040.
[40] Y. Li, et al., ACS RSC Adv. 11 (2021) 26855–26875. DOI:1039/D1RA05796K.
[41] J. Yang, et al., J. Mat. Chem. C. 8 (2020) 2579–2588, https://doi.org/10.1039/c9tc05752h.
[42] J. Hu, et al., Chemosphere 220 (2019) 77–85, https://doi.org/10.1016/j.chemosphere.2018.12.085.
[43] J. Wang, et al., Optik 204 (2020) 164149, https://doi.org/10.1016/j.ijleo.2019.164149.
[44] E. Falletta, et al., ACS Photonics 10 (11) (2023) 3929–3943, https://doi.org/10.1021/acsphotonics.3c00724.
[45] N. Guglielmi, Electro Soc. 119 (1972) 1009, https://doi.org/10.1149/1.2404383.
[46] Y. Fukunaka, et al., J. Electrochem. Soc. 141 (1994) 1783, https://doi.org/10.1149/1.2055005.
[47] C. Chen-Wei, et al., Soc, J. Electrochem. 164 (2017), https://doi.org/10.1149/2.0041708.
[48] K. Ishida, et al., Bull. Alloy Phase Diagr. 11 (1990) 555–560, https://doi.org/10.1007/BF02841716.
[49] W. Melville, Transaction of Faraday Society 32 , 1936, 10.1039/TF9363201026.
[50] D.H. Ha, et al., J. Mater. Chem. 21 (2011) 11498–11510, https://doi.org/10.1039/c1jm10337g.
[51] Ross C.A. *et al.,* MRS Online Proceed. Library, 1990, 205, 239-244, DOI:10.1557/PROC-205-239.
[52] W. Maneeprakorn, et al., J. Mater. Chem. 20 (2010) 2329–2335. DOI:110.1039/b922804g.
[53] M. Zeinali-Rad, et al., J. Mater. Eng. Perf. 24 (2015) 3209–3217, https://doi.org/10.1007/s11665-015-1599-6.
[54] C.W. Chiu, et al., J. Electrochem. Soc. 164 (2017), https://doi.org/10.1149/2.0041708jes.
[55] X. Li, et al., Inter. J. Hydrog. Ener. 45 (21) (2020) 21422–21430, https://doi.org/10.1016/j.ijhydene.2020.05.213.
[56] E. Popczun, et al., . Cem. Inter. Ed. 53 (21) (2014) 5427–5430, https://doi.org/10.1002/anie.201402646.
[57] E. Popczun, et al., J. Mater. Chem. A 3 (2015) 5420–5425, https://doi.org/10.1039/c4ta06642a.
[58] J. Wu, et al., Small 16 (2019) 1900550, https://doi.org/10.1002/smll.201900550.
[59] J. Tian, et al., J. Am. Chem. Soc. 136 (21) (2015) 7587–7590, https://doi.org/10.1021/ja503372r.
[60] A. Sumboja, et al., ACS Appl. Mater. Inter. 10 (18) (2018) 15673–15680, https://doi.org/10.1021/acsami.8b01491.
[61] Z. Huang, et al., Nano Enery 9 (2014) 373–382, https://doi.org/10.1016/j.nanoen.2014.08.013.
[62] R. Deng, et al., Appl. Surf. Sci. 616 (2023), 156456 10.1016/j.apsusc.2023.156456.
[63] M. Wei, et al., Chem. Phy. Lett. 681 (2017) 90–94, https://doi.org/10.1016/j.cplett.2017.05.060.
[64] N. Jiang, et al., . Cem. Inter. Ed. 54 (21) (2015) 6251–6254, https://doi.org/10.1002/anie.201501616.
[65] C. Sihai, et al., Nanotechnology 20 (2009) 275702, https://doi.org/10.1088/0957-4484/20/27/275702.
[66] J. Cao, et al., Appl. Surf. Sci. 284 (2013) 263–269, https://doi.org/10.1016/j.apsusc.2013.07.092.
[67] E.N. Bakatula, et al., Environ. Sci. Pollut. Res 25 (2018) 7823–7833, https://doi.org/10.1007/s11356-017-1115-7.
[68] M. Panizza, et al., Electrochem. Commun. 37 (2001) 336–339, https://doi.org/10.1016/S1388-2481(01)00166-7.
[69] S. Shetty, J. Electro Chem. 796 (2017) 57–65, https://doi.org/10.1016/j.jelechem.2017.05.002.
[70] L. Codognoto, et al., J. Appl. Electrochem. 33 (2003) 951–957, https://doi.org/10.1023/A:1025820029412.
[71] E. Brillas, et al., Chemosphere 79 (6) (2010) 605–612, https://doi.org/10.1016/j.chemosphere.2010.03.004.
[72] H.R. Ghatak, Env. Tec. 35 (19) (2014) 2483–2492, https://doi.org/10.1080/09593330.2014.911357.
[73] F.W. Sifuna, et al., J. Environ. Sci. Health A Tox. Hazard. Environ. Eng. 51 (11) (2016) 954–961, https://doi.org/10.1080/10934529.2016.1191814.
[74] X. Zhao, et al., Electo Acta 54 (17) (2009) 4172–4179, https://doi.org/10.1016/j.electacta.2009.02.059.
[75] G. Mascolo, et al., J. Chromatogr. A 1067 (1-2) (2005) 191–196, https://doi.org/10.1016/j.chroma.2004.12.058.
[76] H. Nadais, et al., Chem. Eng. J. 338 (2018) 401–410, https://doi.org/10.1016/j.cej.2018.01.014.
[77] M.G. Fernandez-Aguirre, et al., Electrochem. Acta 354 (2020) 136686, https://doi.org/10.1016/j.electacta.2020.136686.
[78] G. Loos, et al., Sep. Pur. Tec. 195 (2018) 184–191, https://doi.org/10.1016/j.seppur.2017.12.009.